Impact of Anisotropic Mesh Adaptation on the Aerothermodynamics of Atmospheric Reentry

Fábio Morgado *, Catarina Garbacz † and Marco Fossati ‡
Aerospace Centre of Excellence, University of Strathclyde, Glasgow, G1 1XJ, United Kingdom

The presence of complex geometries and/or multiple bodies during atmospheric re-entry may lead to complex and directional flow features such as shock waves and shear layers that need to be correctly predicted to ensure accurate calculation of the aerothermal loads during re-entry. Central in ensuring reliable numerical prediction of loads is the adoption of meshes that ensure grid independence and minimize the misalignment between the directional flow features and the grid cells interfaces, a situation that is known to give rise to nonphysical behaviours and spurious oscillations. The use of anisotropic unstructured grid adaptation is here presented as a means to ensure appropriate grid resolution and alignment with directional flow features for cases where the use of structured grids is not always possible or practical. Results highlight the effectiveness and reliability of anisotropic mesh adaptation in successfully predicting the location of shock discontinuities as well as surface aerothermodynamic quantities while providing results comparable with established approaches relying on structured meshes. Results are presented for single and multiple bodies cases through comparison with experimental data and reference numerical solutions.

I. Introduction

The accurate simulation of multi-body atmospheric re-entry is a difficult task as a consequence of complex physics such as chemical reactions and excitation of internal degrees of freedom and the presence of complex time-varying geometries and multiple objects that may give rise to intricate flow features and shock impingement on the surface of the bodies, resulting in severe localized aerothermal loads that can lead to fragmentation and affect the body dynamics. Accurately computing the aerothermal loads requires not only the correct assessment of temperature gradients at the object's surface but also the correct flow properties in the post-shock region outside the boundary layer since these will directly impact the near-wall properties.

It is known that the quality of the grid plays an important role on the overall accuracy of the solution. In addition to

*PhD student, Department Mechanical and Aerospace Engineering, AIAA Member, fabio.pereira-morgado@strath.ac.uk.
†PhD student, Department Mechanical and Aerospace Engineering, AIAA Member, ana.gomes@strath.ac.uk.
‡Associate Professor, Department Mechanical and Aerospace Engineering, AIAA Member, marco.fossati@strath.ac.uk.

This is a peer reviewed, accepted author manuscript of the following research article: Morgado, F., Garbacz, C., & Fossati, M. (2022). Impact of anisotropic mesh adaptation on the aerothermodynamics of atmospheric reentry. AIAA Journal, 60(7), 1-17. https://doi.org/10.2514/1.j061071

mesh resolution at local high-gradient regions, one critical factor is the orientation of the cells' interface with respect to directional flow features such as shock waves, contact discontinuities and boundary layers. An adequate resolution of the boundary layer in the surface-normal direction and a good capture of the shock wave must be ensured. If the cells' interfaces are not aligned with the shock discontinuity, the inviscid flux formulation may lead to large entropy errors that are propagated downstream and contaminate the solution near the surface [1]. This issue becomes more obvious in the stagnation region of blunt bodies, where there is little dissipation of entropy gradients and, in some cases, carbuncle phenomena may occur. Several studies have shown that the use of quadrilateral and hexahedral meshes achieves the best results when it comes to shock-capturing and preventing carbuncle phenomena for blunt-body simulations, while triangular and tetrahedral meshes perform the worst [1–4]. It is rather challenging to align the interfaces of a tetrahedral cell with the shock discontinuity, leading to larger discretization errors and non-preservation of the flow symmetry. Gnoffo et al. [4] analysed the possibility of using a fully unstructured uniformly biased tetrahedral mesh with Roe scheme and concluded that, although it's possible to have a good pressure distribution, the heat transfer in the stagnation region is poorly predicted and the accuracy can only be improved by carefully limiting the eigenvalues and through grid refinement. Candler et al. [1] and Nompelis et al. [5] have shown that the post-shock entropy error is a result of grid misalignment with the shock. The use of a tetrahedral grid not aligned with the bow shock causes the injection of spurious momentum into the flowfield which cannot be removed, resulting in poor aeroheating prediction using conventional upwind CFD methods. However, the solution can be partially recovered through the use of quadrilateral/hexahedral elements at the boundary layer region.

Even though the use of structured grids reduces the misalignment error, it is not always a practical solution when simulating hypersonic flows with complex time-varying geometries. The presence of multiple features and their interaction impose great challenges in the generation of a structured grid capable of providing acceptable results, mostly due to topological restrictions [6]. Additionally, if dynamics needs to be accounted and no grid deformation tool is available, the computational grid must be regenerated to consider the objects new position, which may have impact in flow features location. Therefore, in the majority of cases, the location of the features and their intersection are not known beforehand, requiring the use of automatic mesh adaptation tools to sharply capture the complex flow field. The adaptation of hexahedral/quadrilateral grids is usually restricted to nodal redistribution, being far less flexible than adaptation schemes for tetrahedral/triangular grids [7]. The benefit of using mesh adaptation for unstructured isotropic grids has already been shown for blunt body objects in rarefied conditions [8, 9]. However, when continuum conditions are considered, the generated shock waves and directional flow features become more intense and characterised by large gradients. The use of triangular/tetrahedral isotropic grids is not a viable option for flows with intense flow features since, the elements are not aligned with the intense shock waves. Although the refinement of this kind of grids may reduce the post-shock error, the latter will still be injected due to the elements misalignment, putting at risk the prediction of accurate aeroheating. Anisotropic adaptation allows to generate refined grids capable of accommodating

the directional flow features given the ability to stretch elements tangentially to the gradient direction and limiting the edges of the mesh that instead are transverse to the shock. Additionally, to obtain a similar level of accuracy with isotropic grids, it would require a larger number of elements, becoming more computationally expensive and without the guarantee that the misalignment of the elements with the shock would not affect the solution.

In this work, the influence of anisotropic grid adaptation on the prediction of flowfield and surface quantities is analysed for hypersonic flows in air as an alternative to structured grids for cases where the structured grid generation/adaptation is not straightforward, such as the case of an atmospheric re-entry. The key point of this work is to demonstrate that the methodology used to produce anisotropic grids, in addition to automatically providing an optimal grid resolution is capable of resolving directional flow features without the introduction of significant numerical errors in the computed solution and to accurate solutions. First, the grid influence on two- and three-dimensional single body cases is analysed. For hypersonic regime simulations, the single objects can be compared to the leading bodies in a multi-body simulation. Then, the case of proximal cylinders is simulated to assess the ability of anisotropic grids to capture the shock-shock interaction and resultant flow features that will influence the aft cylinder surface quantities, which was carefully placed so that a shock-shock interaction happens in the vicinity of the body. Lastly, a three-dimensional proximal spheres test case is simulated to demonstrate the effectiveness of the approach in 3D cases with multiple bodies. The manuscript is organized as follows: the solver methodology and governing equations are briefly described in the first section, followed by a description of the coupled grid adaptation tool. Numerical tests are discussed in Section IV and finally, a brief summary of the main conclusions is presented.

II. The open-source solver SU2-NEMO

The open-source software suite SU2 [10] has been developed with the purpose of performing high-fidelity analysis of partial differential equations (PDE) and creation of PDE-constrained systems. The suite was mostly written in C++, allowing the construction of high-level object-oriented structures and promoting code re-usability and flexibility to effortlessly integrate new state-of-the-art features. In the past few years, new numerical methods, tools and solvers have been gradually incorporated into the SU2 infrastructure. The requirement of simulating chemically-reactive multi-species and non-equilibrium flows led to the development of the SU2-NEMO (Non-Equilibrium MOdels) solver [11, 12]. The thermochemistry models used in SU2-NEMO are provided through coupling of the solver with the Mutation++ library [13]. The use of the library ensures an appropriate closure of the governing equations for a wide range of temperatures and the use of multi-temperature models for non-equilibrium flows, with the aid of high-fidelity physical models. The coupling has been thoroughly validated [14]. The library has the ability to efficiently compute the thermodynamic, transport and chemical kinetic gas properties for any given custom mixture. The transport properties are computed using binary collision integral mixing methods (Gupta-Yos and Wilke) or the Chapman-Enskog relations. With the exception of the single sphere case, where a perfect gas and a single temperature model was considered, the

dynamic viscosity and thermal conductivity of the remaining cases are computed using a multi-scale Chapman-Enskog perturbative solution of the Boltzman equation [13].

SU2 and SU2-NEMO adopt a classical edge-based Finite Volume Method (FVM) approach for the numerical discretization of the computational domain. Several upwind schemes can be chosen for the calculation of the inviscid fluxes, with special focus on the flux vector splitting (FVS) schemes. To enhance accuracy, the solution is reconstructed using MUSCL (Monotonic Upstream-centered Scheme for Conservation Laws) with the Venkatakrishnan-Wang limiter. The viscous flux is calculated using the average values at the dual-grid interface and the gradient information is retrieved using the Weighted Least-Squares approach.

A. Governing equations and physical models

While SU2 uses the conventional Navier-Stokes equations with a single temperature, the governing equations in SU2-NEMO are obtained by extending the classical Navier-Stokes equations to account for a chemically-reacting, non-equilibrium flow using the two-temperature model by Park [15]. Using this model, the translational energy mode is assumed to be at equilibrium with the rotational mode, while the vibrational mode is assumed to be at equilibrium with the electronic mode. The equations can be written as

$$\frac{\mathrm{d}\mathbf{U}}{\mathrm{d}t} + \nabla \cdot \mathbf{F}^{\mathbf{i}}(\mathbf{U}) - \nabla \cdot \mathbf{F}^{\mathbf{v}}(\mathbf{U}) = \mathbf{Q}(\mathbf{U}), \tag{1}$$

where $\mathbf{U}$ are the conservative variables, $\mathbf{Q}$ are the source terms, $\mathbf{F}^{\mathbf{i}}$ and $\mathbf{F}^{\mathbf{v}}$ are the inviscid and viscous fluxes, respectively. The vectors are given by

$$\mathbf{U} = \begin{Bmatrix} \rho_1 \\ \vdots \\ \rho_{n_s} \\ \rho\mathbf{u} \\ \rho e \\ \rho e^{\text{v-e}} \end{Bmatrix}, \quad \mathbf{F}^{\mathbf{i}} = \begin{Bmatrix} \rho_1\mathbf{u} \\ \vdots \\ \rho_{n_s}\mathbf{u} \\ \rho\mathbf{u}\otimes\mathbf{u} + p\bar{I} \\ \rho\mathbf{u}h \\ \rho\mathbf{u}e^{\text{v-e}} \end{Bmatrix}, \quad \mathbf{F}^{\mathbf{v}} = \begin{Bmatrix} \mathbf{J}_1 \\ \vdots \\ \mathbf{J}_{n_s} \\ \bar{\tau} \\ \bar{\tau}\cdot\mathbf{u} + \sum_s \mathbf{J}_s h_s + \mathbf{q}^{\text{t-r}} + \mathbf{q}^{\text{v-e}} \\ \sum_s \mathbf{J}_s h_s^{\text{v-e}} + \mathbf{q}^{\text{v-e}} \end{Bmatrix}, \quad \mathbf{Q} = \begin{Bmatrix} \dot{\omega}_1 \\ \vdots \\ \dot{\omega}_{n_s} \\ 0 \\ 0 \\ \dot{\Omega} \end{Bmatrix}, \tag{2}$$

in which ρ is the density, $\mathbf{u}$ is the velocity vector, p is the static pressure, h is the total enthalpy per unit mass of the mixture, e is the energy per unit mass, $\bar{\tau}$ is the viscous stress tensor, $\mathbf{q}$ is the conduction heat flux, $\mathbf{J}$ is the mass diffusion flux, $\dot{\omega}$ is the net rate of species production, $\dot{\Omega}$ is the source term of vibrational energy and n_s is the number of species in the mixture. The subscript index s stands for the s^{th} chemical species in the mixture and the superscript t-r and v-e stand for the translational-rotational and vibrational-electronic modes, respectively. If the quantity does not have a subscript,

it is related to the full mixture. The term $\bar{I}$ denotes the identity matrix.

Individual chemical species are assumed to behave as an ideal gas. Under this assumption, the total pressure of the mixture is defined using Dalton's law as

$$p = \sum_{s=1}^{n_s} p_s, \tag{3}$$

where p_s is the partial pressure of each species. The partial pressure can be determined by using the ideal gas law

$$p_s = \rho_s \frac{R_\mathrm{u}}{M_s} T_\mathrm{tr}, \tag{4}$$

where R_u is the universal gas constant, M_s is the molar mass of species s and T_{tr} is the translational-rotational temperature of the mixture. The total specific energy of the flow is given as the sum of the internal and kinetic energies

$$e = \sum_{s=1}^{n_s} c_s e_s + \frac{1}{2}|\mathbf{u}|^2, \tag{5}$$

where c_s is the mass fraction of species s, $|\mathbf{u}|$ is the magnitude of the flow velocity vector and e_s is the specific internal energy of the species, given by

$$e_s = e_s^\mathrm{t}(T_\mathrm{tr}) + e_s^\mathrm{r}(T_\mathrm{tr}) + e_s^\mathrm{v}(T_\mathrm{ve}) + e_s^\mathrm{e}(T_\mathrm{ve}) + e_s^0. \tag{6}$$

where e_s^0 is the energy of formation, e_s^t, e_s^r, e_s^v and e_s^e are the translational, rotational, vibrational and electronic energy contribution, respectively. The thermal nonequilibrium calculations are performed using the Rigid-Rotor/Harmonic-Oscillator (RRHO) model.

To account for the species production and destruction caused by the occurring chemical processes, the species source term $\dot{\omega}_s$ are included in the conservative equations, which are given by

$$\dot{\omega}_s = M_s \sum_{r=1}^{n_r} (\nu''_{s,r} - \nu'_{s,r}) \left[k_{\mathrm{f},r} \prod_{j=1}^{n_s} \hat{\rho}_j^{\nu'_{j,r}} - k_{\mathrm{b},r} \prod_{j=1}^{n_s} \hat{\rho}_j^{\nu''_{j,r}} \right], \tag{7}$$

where n_r and n_s are the number of reactions r and the number of species s, respectively, ν'_s is the forward reaction stoichiometry coefficient, ν''_s is the backward reaction stoichiometry coefficient, $\hat{\rho}_j$ is the molar density, $k_{\mathrm{f},r}$ is the forward reaction rate and $k_{\mathrm{b},r}$ is the backward reaction rate.

B. Inviscid Flux Scheme

This work's simulations were performed using the newly implemented AUSM+M scheme, proposed to increase robustness and performance for all speeds. This accomplishment is the result of three new key formulations: pressure

diffusion term for mass flux, velocity diffusion term for pressure flux and numerical sound speed.

The AUSM+M scheme follows the general governing equations of the AUSM family with a few modifications. The inviscid flux is expressed as

$$\mathbf{F}_{1/2} = \frac{\dot{m} + |\dot{m}|}{2}\boldsymbol{\phi}_L + \frac{\dot{m} - |\dot{m}|}{2}\boldsymbol{\phi}_R + \mathbf{P}_{1/2}, \tag{8}$$

$$\boldsymbol{\phi} = \begin{Bmatrix} 1 \\ \mathbf{u} \\ h \\ e^{\text{v-e}} \end{Bmatrix}, \quad \mathbf{P}_{1/2} = \begin{Bmatrix} 0 \\ p_s \bar{I} \cdot \mathbf{n} + \mathbf{p}_{\mathbf{u_n}} \\ 0 \\ 0 \end{Bmatrix}, \quad \dot{m} = M_{1/2} c_{1/2} \begin{cases} \rho_L & \text{if } M_{1/2} \geq 0; \\ \rho_R & \text{if } M_{1/2} < 0; \end{cases} \tag{9}$$

where $\dot{m}$ is the mass flux, $\mathbf{P}_{1/2}$ is the pressure flux, p_s is the interface pressure, p_u is the velocity diffusion term, and $c_{1/2}$ and $M_{1/2}$ are the value of the numerical sound speed and Mach number at interface, respectively. The numerical sound speed is calculated using the definition suggested by Kim et al. [16] in order to satisfy the Prandtl relation across oblique shocks.

The interface Mach number is calculated using a new formulation for the pressure diffusion term M_p

$$M_{1/2} = M_{\mathrm{L}}^{+} + M_{\mathrm{R}}^{-} + M_{\mathrm{p}}, \tag{10}$$

$$M_{\mathrm{p}} = -(1 - f)(1 - g)\frac{1}{2}\frac{p_R - p_L}{\rho_{1/2} c_{1/2}^2}. \tag{11}$$

The subscripts "L" and "R" and superscripts "+" and "-" stand for the left and right states across the cell interface, respectively. The split Mach numbers M_L^+ and M_R^- are calculated using the same approach as in the AUSM+UP scheme [17]. The term g is the multidimensional pressure-based sensing function [18] used to detect strong shock wave and to preserve shear layers and the term f is the Mach number limiting function used for a good transition through all range of speeds. The functions are expressed as

$$g = \frac{1 + \cos(\pi h)}{2}, \quad h = \min_k(h_k), \quad h_k = \min\left(\frac{P_{\mathrm{Lk}}}{P_{\mathrm{Rk}}}, \frac{P_{\mathrm{Rk}}}{P_{\mathrm{Lk}}}\right), \quad \text{and} \tag{12}$$

$$f = \frac{1 - \cos(\pi M)}{2}, \quad M = \min(1, \max(|M_L|, |M_R|)), \tag{13}$$

where the index k indicates the adjacent interfaces for both cells being evaluated. The interface pressure is calculated

using

$$p_s = \frac{p_L + p_R}{2} + (\psi_L^+ - \psi_R^-)\frac{p_L - p_R}{2} + f_o(\psi_L^+ + \psi_R^- - 1)\frac{p_L + p_R}{2}, \tag{14}$$

$$f_o = \min(1, \max(f, M_\infty^2)), \tag{15}$$

where the function f_o is a scaling Mach number function dependent of function f defined in equation 13. The term M_∞ is the free-stream Mach number and the terms ψ_L^+ and ψ_R^- are the pressure splitting functions used in the AUSM+UP scheme. In order to avoid the propagation of perturbation and occurrence of carbuncle, an additional dissipation mechanism is implemented in AUSM+M. The velocity diffusion is expressed as

$$p_{u_\mathbf{n}} = -g \cdot \frac{\gamma(p_L + p_R)}{2c_{1/2}}\psi_L^+\psi_R^-(u_{R_\mathbf{n}} - u_{L_\mathbf{n}}). \tag{16}$$

where $u_{R/L_\mathbf{n}}$ is the velocity component in the $\mathbf{n}$ direction.

III. Adaptive Mesh Generation

The pyAMG library developed by the GAMMA team at INRIA * [19–21] is used to generate the anisotropic grids for this work test cases by coupling the SU2 solver and the AMG mesh adaptation tool via python interface. The pyAMG software is a python wrapper for the Adaptive Mesh Generation library (AMG-lib), a fast and robust mesh adaptation tool capable of generating anisotropic grids around 2D and 3D complex geometries. The local anisotropic elements follow the direction of the complex multi-directional flow features, such as shock waves, contact discontinuities and boundary layers. This is done by computing an optimal Riemannian metric tensor field from the error estimate of a given background mesh and respective flowfield solution, containing information of the elements edge size and orientation for the adaptation process. The adaptation process will use the Riemannian metric tensor to compute edge lengths and will perform nodes insertion, nodes deletion and nodes movement to achieve a uniform mesh in the Riemannian space. The aim is to achieve error equidistribution over the computational domain. An isotropic mesh in the Riemannian space will appear anisotropic in the classical Euclidean space.

The computed interpolation error is second-order in space and can be approximated using the Hessian matrix $H(\mathbf{x})$, calculated using a double $\mathbf{L}^2$-projection [22]. To ensure that the computed metric field is positive definite, the absolute value of the Hessian matrix is used, given as

$$|\mathcal{H}| = \mathcal{R}\,|\Lambda|\,\mathcal{R}^\mathsf{T}. \tag{17}$$

*https://pyamg.saclay.inria.fr/

The Riemannian metric field used to obtain the final grid is given by the $\mathbf{L}^p$-norm normalization of the Hessian matrix for a mesh complexity constraint $\mathcal{N}$ specified before the adaptation process:

$$\mathcal{M}(\mathbf{x}) = \mathcal{N}^{\frac{2}{3}} \left(\int_{\Omega} (\det |H(\mathbf{x})|)^{\frac{p}{2p+3}} \, \mathrm{d}\Omega \right)^{-\frac{2}{3}} (\det |H(\mathbf{x})|)^{-\frac{1}{2p+3}} \, |H(\mathbf{x})| \tag{18}$$

where $\mathcal{N}$ is a measure of the desired number of Degrees Of Freedom (DOFs) in the final adapted mesh, $\left(\int_{\Omega} (\det |H(\mathbf{x})|)^{\frac{p}{2p+3}} \, \mathrm{d}\Omega \right)^{-\frac{2}{3}}$ is a global normalization used to reach the desired number of DOFs, and $(\det |H(\mathbf{x})|)^{-\frac{1}{2p+3}}$ is a local normalization to assess the sensitivity to small variations.The choice of the norm impacts the adaptation procedure. For example, the $\mathbf{L}^1$-norm can be used to better capture small amplitude variations and has been shown to be effective for supersonic applications [23]. Additionally, the choice of the sensors used to compute the interpolation error also have an impact on the adaptation process. As an example, using pressure as sensor does not ensure an adequate grid adaptation at the boundary layer region due to the presence of small pressure gradients near the object surface. The pyAMG tool recursively uses anisotropic local operators to equidistribute the interpolation error, such as point insertion, edge swapping, edge collapse and point smoothing, improving the output grid through the computed metric field and imposing quality constraints to guarantee the robustness and quality of the final grid [24].

For the test cases considered in this work, the total overhead cost associated to the mesh adaptation process has been assessed by evaluating the ratio of the total time spent for adapting the mesh plus interpolating a solution onto the new mesh and the total time required to obtain a grid independent solution from the initial non-adapted mesh. Considering three adaptation levels, the overhead cost on average has been estimated to be 0.0001% of the total simulation time. All the adaptation steps were performed considering Mach number as a sensor, i.e., pyAMG used the Mach number interpolation error metric tensor to generate the anisotropic grid.

IV. Numerical Results

The test cases were simulated with the SU2-NEMO [12] solver to assess the effect of grid element type and orientation on the solution obtained with anisotropic unstructured grids (2D and 3D cases) and fully structured grids (2D cases only). First, a single isolated two-dimensional cylinder and three-dimensional sphere are analysed and results are compared with the available reference data in literature. These isolated blunt bodies generate a single shock wave without any interaction with other flow features, thus enabling to analyse in greater detail the effects of grid misalignment with the shock and the generation of momentum in the wrong direction. Additionally, for the case of the single cylinder, a comparison with the solution obtained from a generated structured grid is also performed, as it is known that the problem of misalignment between the shock and the mesh is known to be less problematic for quadrilateral/hexahedral grids.

After demonstrating the use of anisotropic grids for flows around single blunt bodies with numerical and experimental

data comparison, two-dimensional proximal cylinders and three-dimensional proximal spheres test cases are examined. The ability of anisotropically adapted grids to achieve good surface predictions and alignment with the different directional flow features generated due to shock-shock interactions is demonstrated. The two-cylinder anisotropic results are compared with the integral quantities from reference literature data and with the results obtained through the generation of a structured grid that closely follow the directional flow features. The three-dimensional proximal spheres results are validated with experimental data provided by DLR Institute of Aerodynamics and Flow Technology through experimentation using the hypersonic wind tunnel H2K [25].

Both inviscid and viscous simulations are conducted for the two-dimensional cases and only viscous simulations for the three-dimensional cases. For the considered viscous cases, it is of major importance to use a structured grid across the boundary layer to overcome surface heating problems introduced by the use of tetrahedral grids in the capture of the bow shock, as shown by Nompelis et al. [5]. The erroneous heating prediction is caused by the introduction of entropy errors when the faces of the local elements are not aligned with the shock, which propagate and contaminate the shock layer [26].

A. 2D Single Cylinder

Let us consider a simulation of a non-equilibrium hypersonic flow past a single cylinder, using the free-stream conditions and mass fractions in Table 1. This non-trivial test case has been used as validation of the physico-chemical models used in CFD solvers [27] since the shock layer is subject to non-equilibrium chemical and vibrational relaxation. The simulations were performed on the two grids shown in Fig. 1 for the inviscid and viscous flow. The grids have the same structured boundary layer grid, with 200 equally spaced elements along the cylinder surface, and 135 elements in the normal direction, starting with a first element height of 1×10^{-8} m from the surface and linearly growing in the normal direction with a progression rate of 1.075. The number of nodes and elements, along with the aspect ratio details can be seen in Table 2.

The structured and the initial isotropic grid used to start the anisotropic grid adaptation were generated using the open-source software GMSH [28], from which the tetrahedral elements were created using the Delaunay triangulation method. The anisotropic adaptation was performed using the Mach number of the steady-state solution to compute the Hessian matrix for the anisotropic metric.

To assess the existence of grid misalignment that may generate numerical issues in the post-shock solution of the anisotropic grid, Fig. 2 compares the velocity component of the stream in the normal direction for both grids, by normalizing it with the value of the post-shock velocity u_2 at the stagnation line for the inviscid case. Candler et al. [1] shows in his work similar comparisons and concludes that the misalignment of the shock with the grid elements induce the formation of momentum in the wrong direction. Candler also mentions that this error rapidly increases with Mach number and that this problem is more severe for triangular/tetrahedral grids. However, when comparing both grids

Table 1 Free-stream and wall values for the single cylinder case.

T_∞ $[K]$	901
T_w $[K]$	300
ρ_∞ $[kg/m^3]$	1.547e-03
U $[m/s]$	5956
N [%]	6.5e-05
O [%]	22.83
NO [%]	1.026
N2 [%]	75.431
O2 [%]	0.713

Table 2 Grid details for the single cylinder case.

Grid	Nodes	Elements	Average AR	Maximum AR	Cores	CPU(h)
Isotropic grid - level 0	166,694	394,534	1.553	1.600	40	114
Anisotropic grid - level 1	244,132	803,567	6.497	35.691	40	104
Anisotropic grid - level 2	339,852	1,329,244	10.767	55.913	40	146
Structured grid	141,000	189,744	—	—	40	80

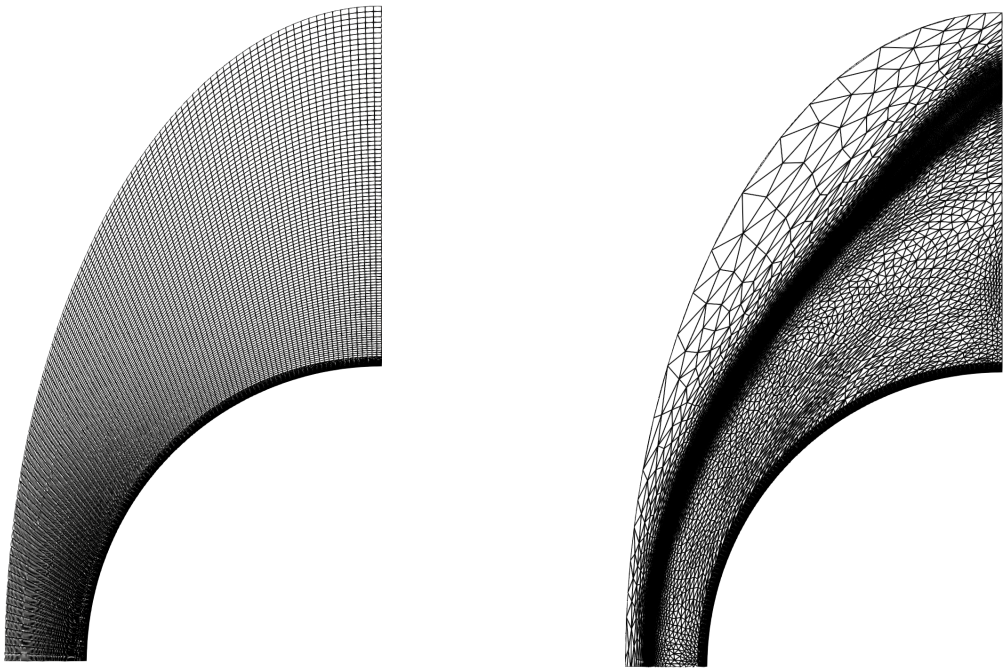

a) Structured b) Unstructured Anisotropic

Fig. 1 Grids overview for the single cylinder case.

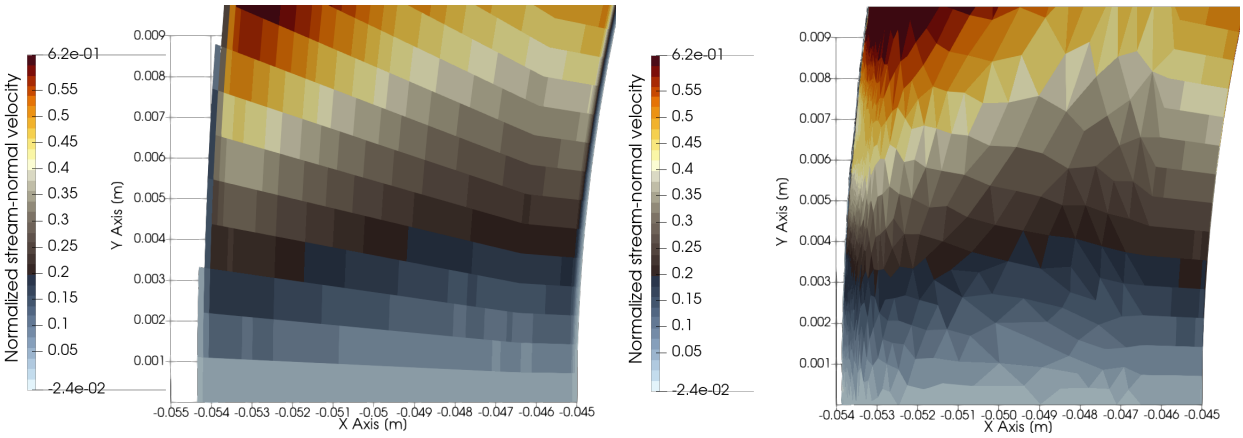

a) Structured b) Unstructured Anisotropic

Fig. 2 Normalized stream-normal velocity (v/u_2) for the single cylinder case with respect to the cylinder center and stagnation line.

results, it is interesting to see that this is not the case for the anisotropic solution. For a better comparison between both grids, the cell-centered value is plotted without smoothing. Both grids present similar values of velocity relatively in the same cell location, with no major spikes of normal momentum generated due to misalignment with the exception of a cell in the anisotropic grid with a minimal velocity error of -0.024u_2, thus indicating that the anisotropic grid is aligned with the intense shock wave generated by the cylinder.

The plot contours of normalized pressure and temperature are illustrated in Fig. 3. By analysing the contour plots, it is clear that the anisotropic grid captures more sharply the shock wave. This result is expected since the anisotropic grid was generated to follow the flow features, while the structured grid was not adapted. Thus, the elements of the structured grid do not strictly follow the shock, which is more noticeable when approaching the outlet boundary. Comparing pressure and temperature contours for both inviscid and viscous formulations, no major difference is noticeable with the exception of the expected shock thickness increase for the viscous case.

The pressure at the surface is plotted in Fig. 4 for the two grids, and compared to experimental data obtained from the High Enthalpy Shock Tunnel Göttingen, HEG [29], using 17 pressure transducers and thermocouples, covering a circumferential angle of ± 60° to measure surface pressure and heat flux distributions. The solution obtained for both grids is in good agreement with the experimental data. For a better comparison between the two grids, only a small region near the stagnation point is considered. Since the solution is not known before the generation of the structured grid, it is not possible to guarantee the local alignment of the structured grid elements with the shock wave as the distance from the stagnation line increases, therefore predicting with higher accuracy the surface quantities near the stagnation point. Both the structured and anisotropic grid show a similar pressure profile.

Similar plots near the stagnation point are obtained for the heat flux distribution in Fig. 5. Once again, the plot only

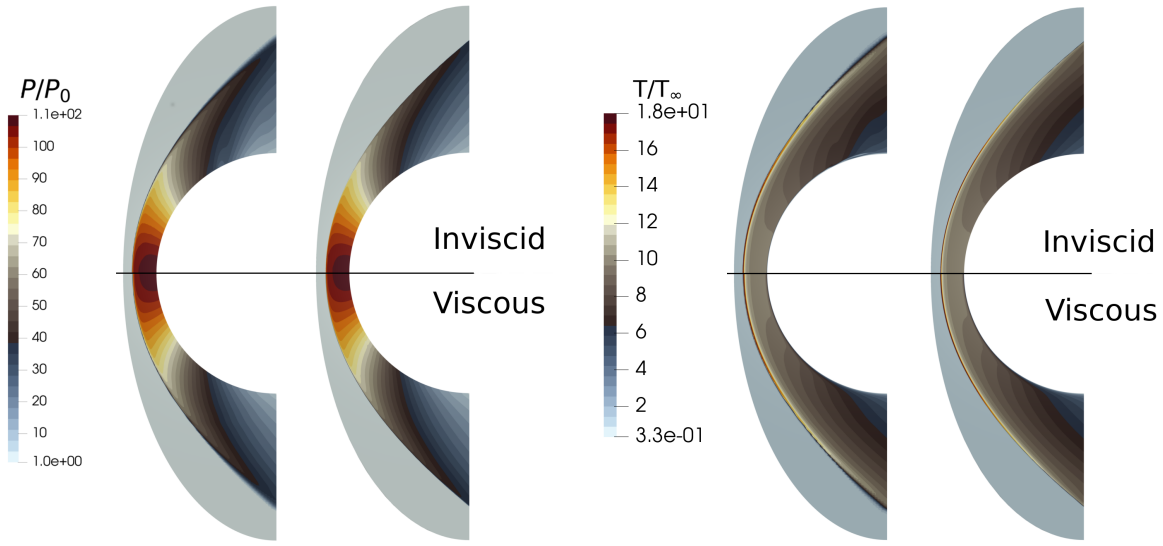

a) Pressure contours b) Temperature contours

Fig. 3 Flow contours of the single cylinder case.

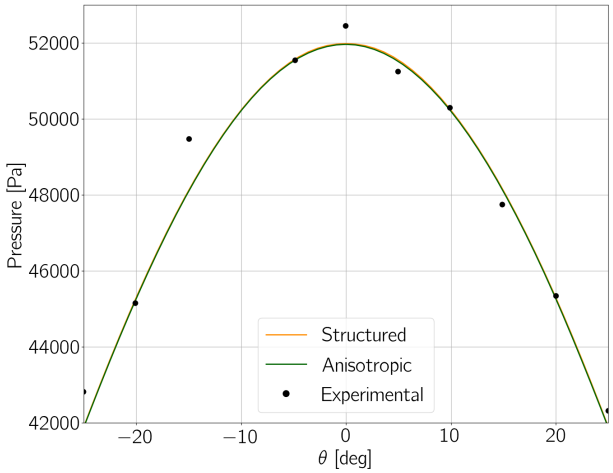

Fig. 4 Surface pressure plot for the single cylinder.

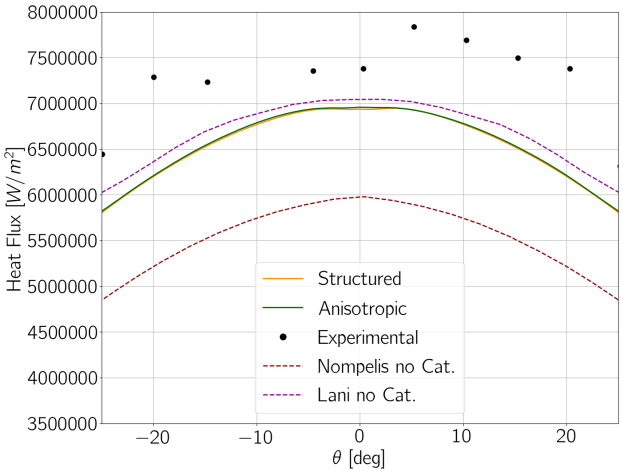

Fig. 5 Surface heat flux plot for the single cylinder.

covers the area near the stagnation region since, from an engineering point of view, it is the most important region to be accurately predicted since the peak values that can lead to structural failure and crack initialization are located there. The results obtained from using an anisotropic grid are identical to the solution from a structured grid. The heat flux distribution from the numerical simulations is underestimated when compared to the experimental data, due to the fact that there is no catalytic effect applied at the wall. Nevertheless, the results obtained in this work are comparable with the non-catalytic simulation results of Andrea Lani and are in better agreement than the results of Nompelis [27].

B. 3D Single Sphere

To further assess how the anisotropic grids handle the prediction of surface pressure and thermal quantities, a three-dimensional flow over a single sphere is considered in this section. The 1 decimeter radius sphere is subjected to the free-stream and boundary conditions shown in Table 3, which correspond to a Mach 12 flow with a Reynolds number of $500,000$. For a better comparison with Candler et al. [1] and Gnoffo et al. [3] results for this particular test case, a perfect gas air model was considered instead of the two-temperature model used in the other test cases. Figure 7 illustrates the evolution of the heat flux and pressure surface contours through the grid adaptation. The details of the grids can be observed in Table 4. All grids have a hexahedrical boundary layer with 80 elements normal to the surface.

Table 3 Free-stream and wall values for the single sphere case.

T_∞ $[K]$	300
T_w $[K]$	800
ρ_∞ $[kg/m^3]$	0.0216
U $[m/s]$	4167

Table 4 Grid details for the single sphere case.

Grid	Nodes	Elements	Average AR	Maximum AR	Cores	CPU(h)
Isotropic grid - level 0	448,754	703,444	1.568	5.503	40	181
Anisotropic grid - level 1	977,849	3,876,455	2.026	11.817	40	521
Anisotropic grid - level 2	1,385,755	6,329,490	4.840	25.591	80	896
Anisotropic grid - level 3	1,955,103	9,744,654	9.652	55.388	80	1325

Similar to Section IV.A, an analysis of the spurious momentum generation near the stagnation line throughout the adaptation levels is shown in Fig. 6. While the first row of sub-figures representing the first anisotropic grid generated contains elements that are clearly introducing wrong values of momentum, it becomes clear that as adaptation progresses, the error is corrected, until the error introduced at the shock area is minimized in the last level of adaptation.

The first row of sub-figures in Fig. 7 shows the surface contours obtained using an unbiased isotropic grid, and illustrates how the non-alignment of the elements in the shock area affect the prediction of the surface loads. While only one level of anisotropic grid adaptation is required to observe vast improvements in the symmetry capture of the surface

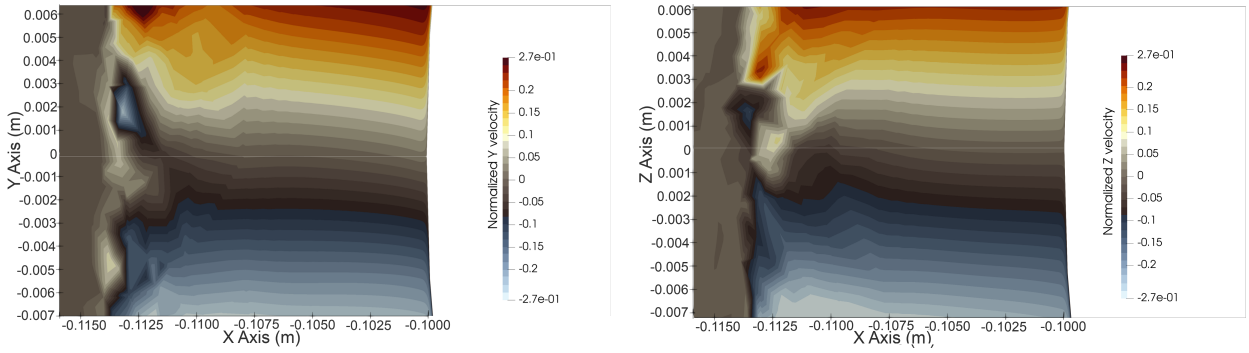

(a) Anisotropic grid - level 1

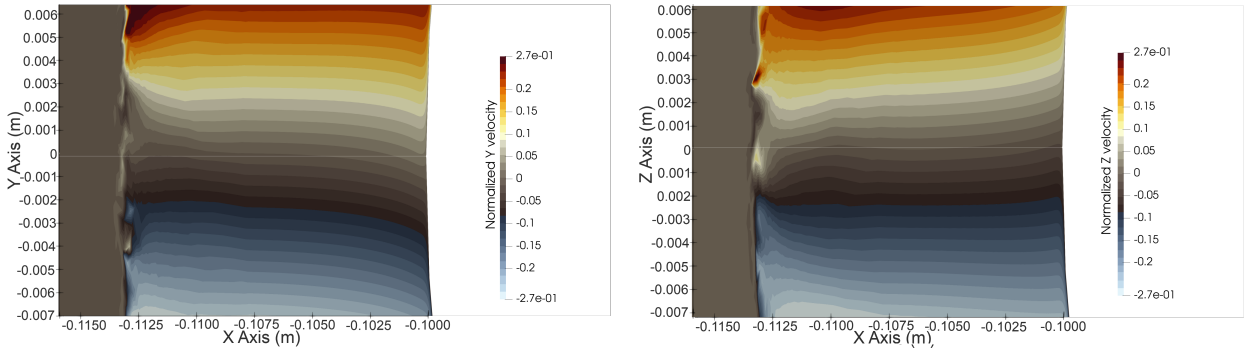

(b) Anisotropic grid - level 2

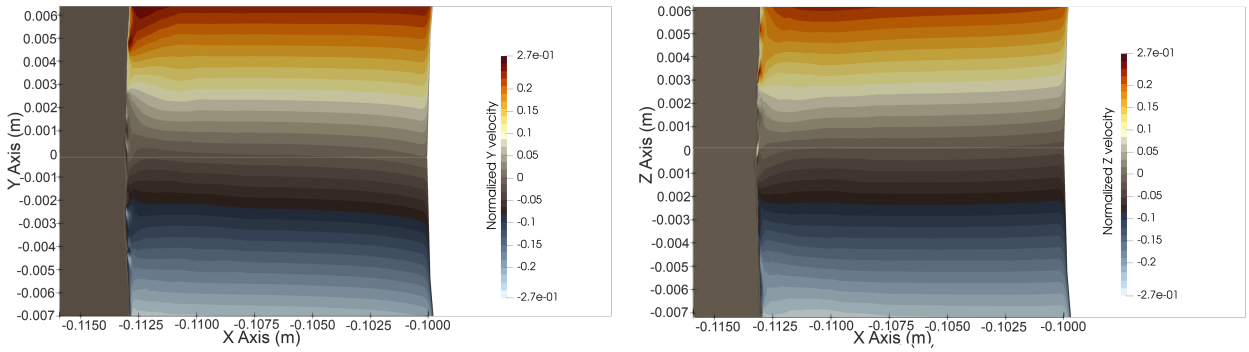

(c) Anisotropic grid - level 3

Fig. 6 Contours of normalized y- velocity $[v/u_2]$ (left) and z- velocity $[w/u_2]$ (right) components contours of the single sphere case for different levels of adaptation with respect to the sphere center and stagnation line.

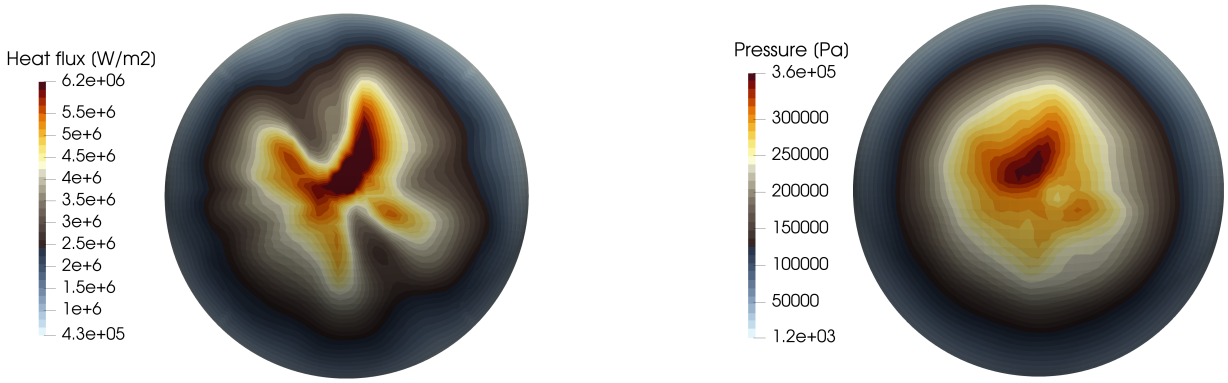

(a) Isotropic grid - level 0

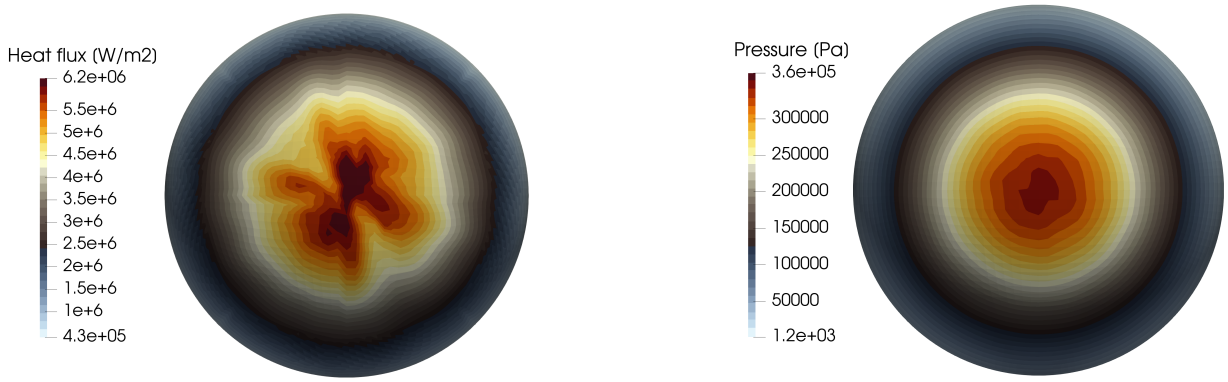

(b) Anisotropic grid - level 1

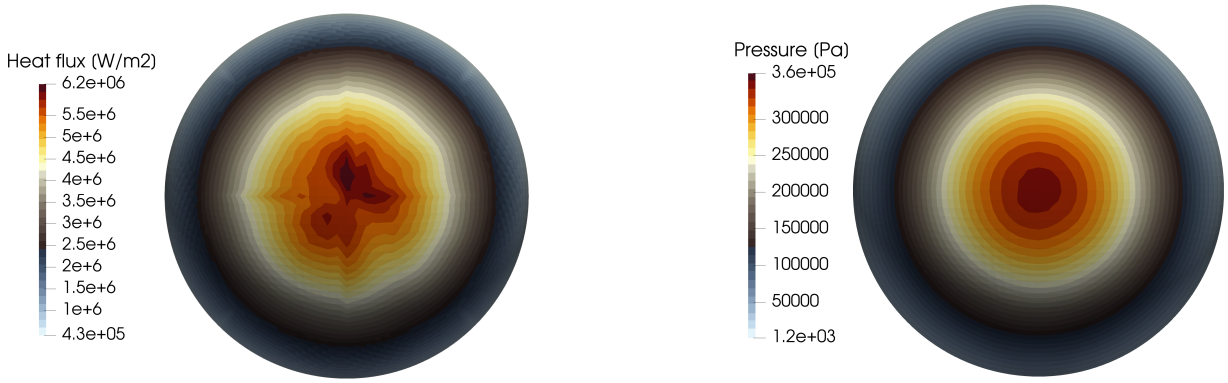

(c) Anisotropic grid - level 2

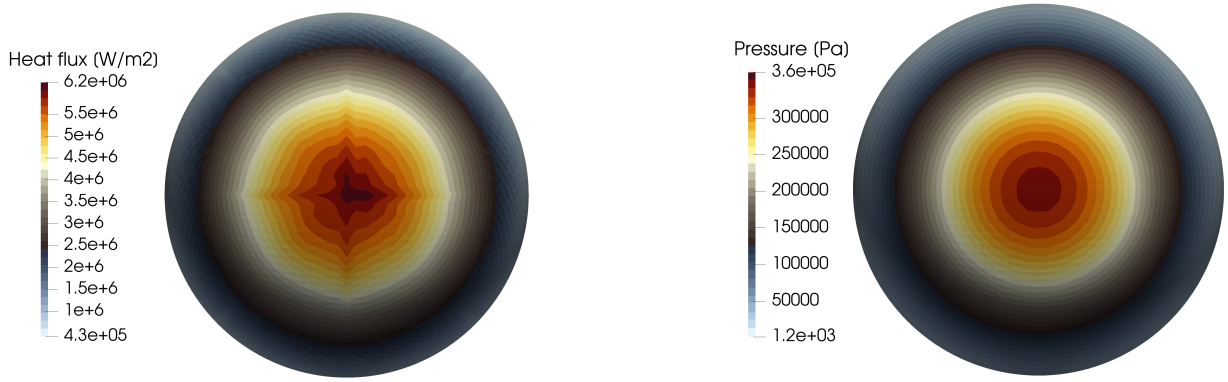

(d) Anisotropic grid - level 3

Fig. 7 Heat flux (left) and pressure (right) contours of the single sphere case for different levels of adaptation.

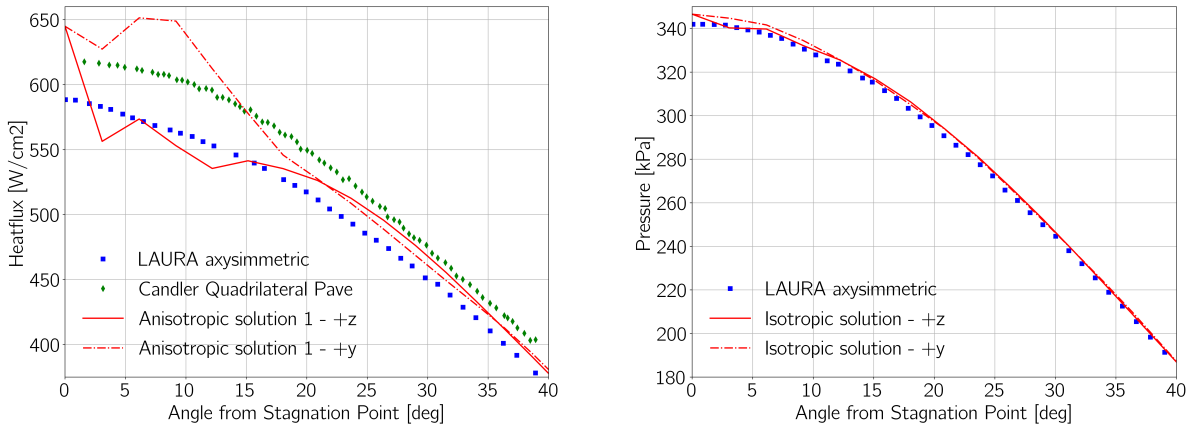

(a) Anisotropic grid - level 1

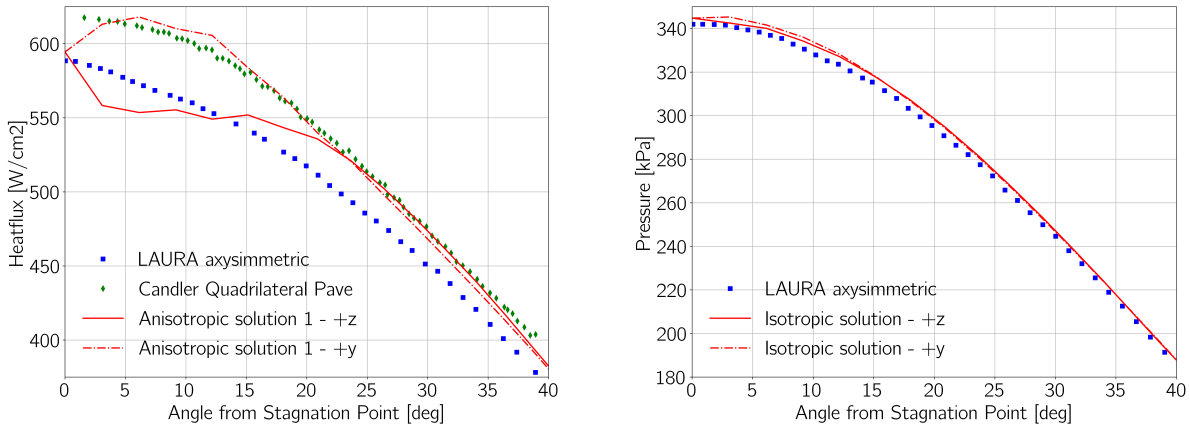

(b) Anisotropic grid - level 2

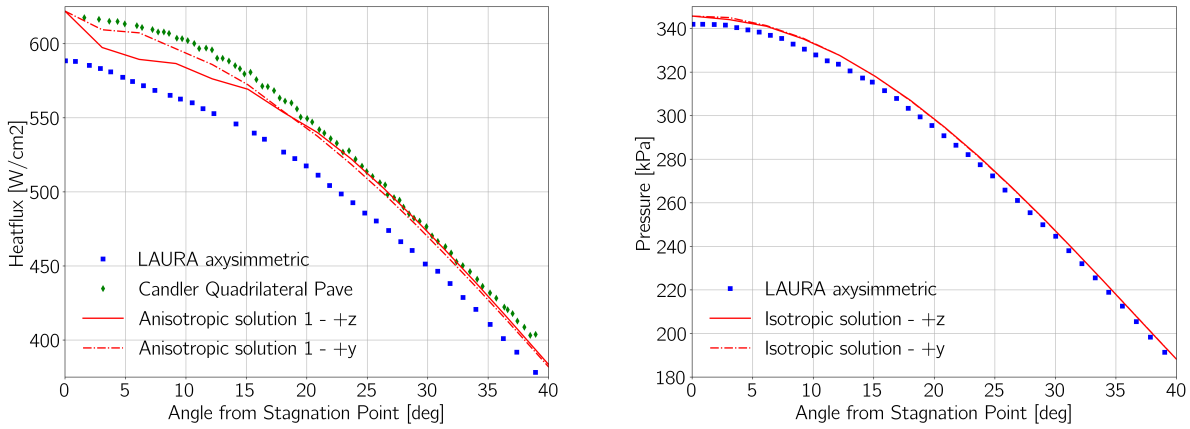

(c) Anisotropic grid - level 3

Fig. 8 Heat flux (left) and pressure (right) plots of the different anisotropic grids for the +y and +z plane.

pressure near the stagnation point, the predicted heating is more sensitive to the local grid orientation at the shock, thus requiring more iterations to obtain a near symmetric solution without the use of flux reconstruction methods [3].

The heat flux and pressure plots (Fig. 8) of the +y and +z plane for the different anisotropic grids show a symmetry improvement throughout the adaptation process. The last row of sub-figures correspond to the plots of the last adapted grid. The plots show that symmetry was achieved in the prediction of surface pressure and, although symmetry was not achieved for the heat flux, the plots show a clear convergence of the heating prediction in the +y and +z plane, and it's comparable with the solution obtained from LAURA [3] and US3D [1] solvers, showing the applicability of anisotropic grids for 3D cases.

C. 2D Proximal Cylinders

The hypersonic flow around a complex vehicle or several bodies often has the presence of multiple shock waves, which are at the origin of shock-shock interactions and shock impingement on the surface of the body. The accurate capture of these interactions is of utter importance to understand how it will affect the aerothermal loads of the objects downstream. In this section, a 2D case of proximal bodies is simulated, using the free-stream conditions in Table 5 and the geometry in Fig. 9, such that the interaction occurs in the vicinity of the aft cylinder.

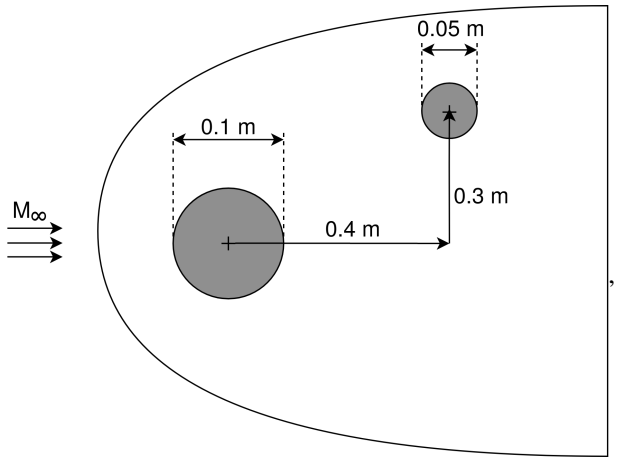

Fig. 9 Geometry configuration of the two-dimensional two-cylinder case

Table 5 Free-stream and wall values of the two-cylinder case.

T_∞ $[K]$	210
T_w $[K]$	300
ρ_∞ $[kg/m^3]$	4.495e-05
U $[m/s]$	2911
N [%]	0
O [%]	0
NO [%]	0
N2 [%]	77
O2 [%]	23

Both Euler and Navier-Stokes simulations were conducted using the grids in Fig. 10 and Fig. 11 respectively, in the regions of interest, i.e., where the shock interaction occurs. The structured grid was generated using the multi-blocks technique, as the position of the shock waves and their interaction were known beforehand. Therefore, the structured blocks were introduced to follow the flow features as aligned as possible. Just like the previous case, the anisotropic grid was created through the adaptation of the isotropic grid. The author has opted to not use a structured boundary layer for the inviscid unstructured meshes, to assess the grid impact on the pressure distribution when compared to the results obtained with the structured mesh. Both grid details are described in table 6 and table 7 for the inviscid and viscous

case, respectively.

Table 6 Grid details for the inviscid proximal cylinder case.

Grid	Nodes	Elements	Average AR	Maximum AR	Cores	CPU(h)
Isotropic grid - level 0	149,652	298,135	1.01	1.68	40	81
Anisotropic grid - level 1	120,388	239,992	5.29	73.948	40	40
Structured grid	478,030	237,900	—	—	40	125

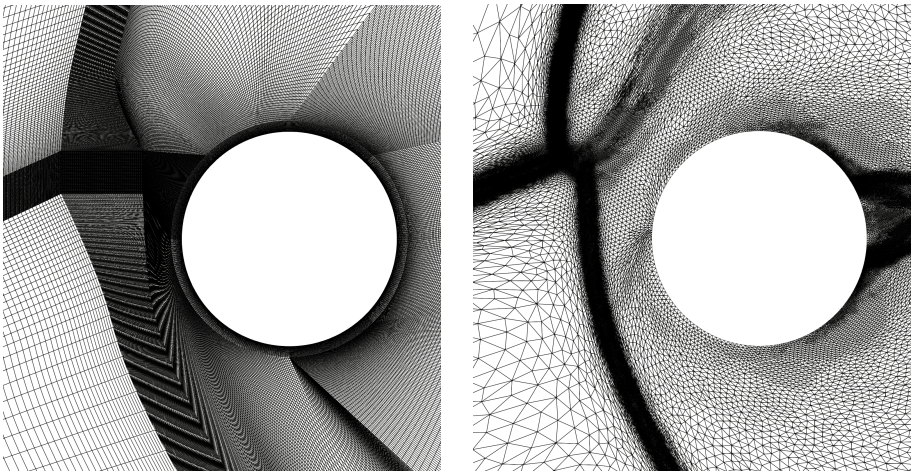

a) Structured b) Unstructured Anisotropic

Fig. 10 Grids overview for the two-cylinder case using inviscid formulation.

Table 7 Grid details for the viscous proximal cylinder case.

Grid	Nodes	Elements	Average AR	Maximum AR	Cores	CPU(h)
Isotropic grid - level 0	578,658	1,657,059	1.556	5.618	40	486
Anisotropic grid - level 1	290,720	698,653	4.623	58.852	40	132
Anisotropic grid - level 2	545,358	1,808,059	6.16	71.780	80	323
Anisotropic grid - level 3	692,845	2,493,869	6.32	77.938	80	445
Structured grid	778,620	516,800	—	—	80	304

The pressure and temperature contours near the aft cylinder for the inviscid case are illustrated in Fig. 12 and Fig. 13, respectively. The shock interaction pattern is sharply captured using both anisotropic and structured grids. The shock-shock interference can be characterized as being of type VII according to the work of Yamamoto et al. [30], where the supersonic jet produced does not strike the body, but follows to the upper downstream region instead. The jet unsteadiness, common for these type of interactions, can be clearly observed for the case of the structured grid. A weaker degree of unsteadiness is also observed for the anisotropic grid.

Comparing the pressure distribution at the cylinder, in Fig. 14, the structured and anisotropic grids have an almost coincident pressure profile. The lift and drag coefficients provided by SU2-NEMO solver using the inviscid formulation

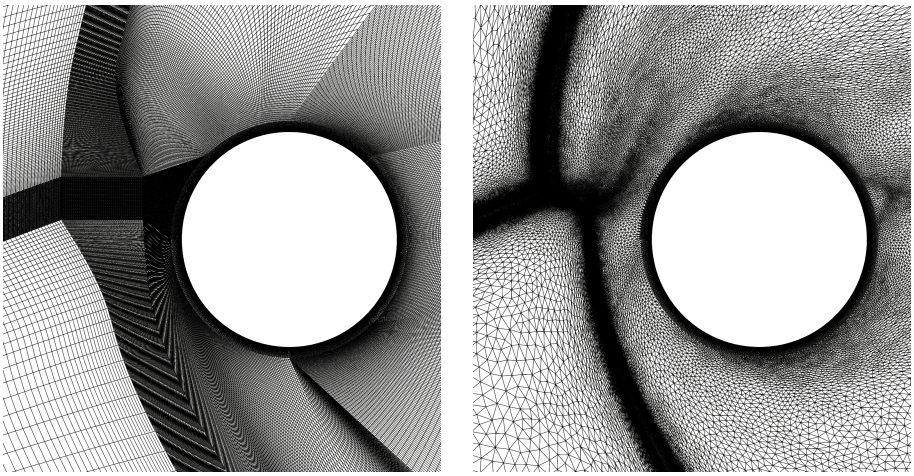

a) Structured b) Unstructured Anisotropic

Fig. 11 Grids overview for the two-cylinder case using viscous formulation.

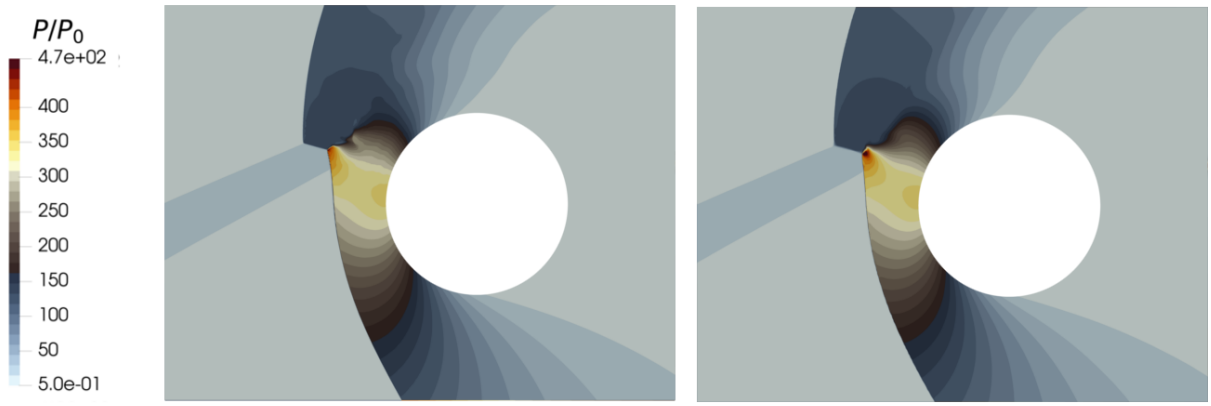

Fig. 12 Normalized pressure contours for the structures and anisotropic grids, respectively, at the shock-shock interference region using inviscid formulation.

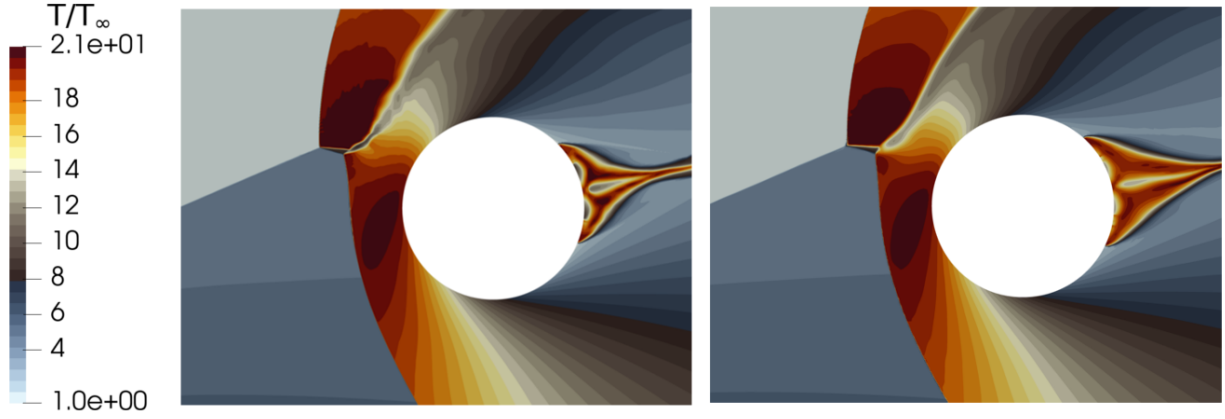

Fig. 13 Normalized temperature contours for the structured and anisotropic grids, respectively, at the shock-shock interference region using inviscid formulation.

with the anisotropic grid are compared to the reference values of Laurence et al. [31] in Fig. 16 and Fig. 17 respectively, showing a perfect agreement with the available data.

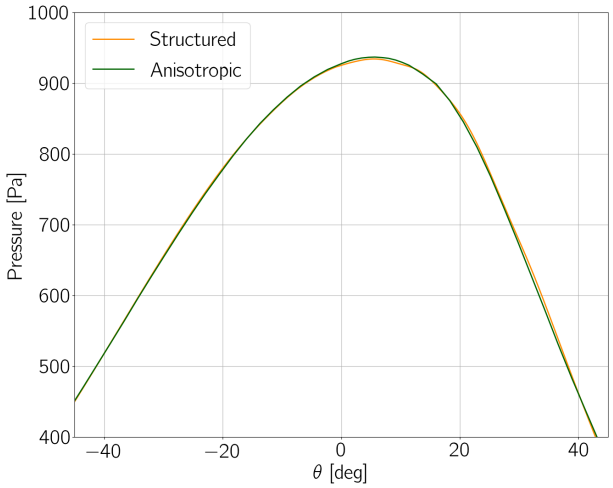

Fig. 14 Surface pressure plot of the aft cylinder for the two-cylinder case using inviscid formulation.

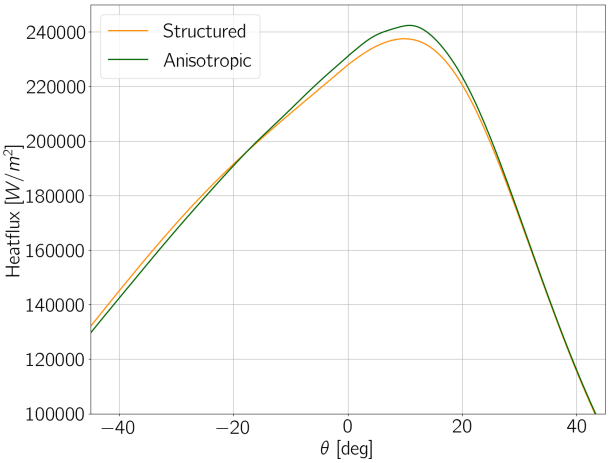

Fig. 15 Surface heat flux plot of the aft cylinder for the two-cylinder case using viscous formulation.

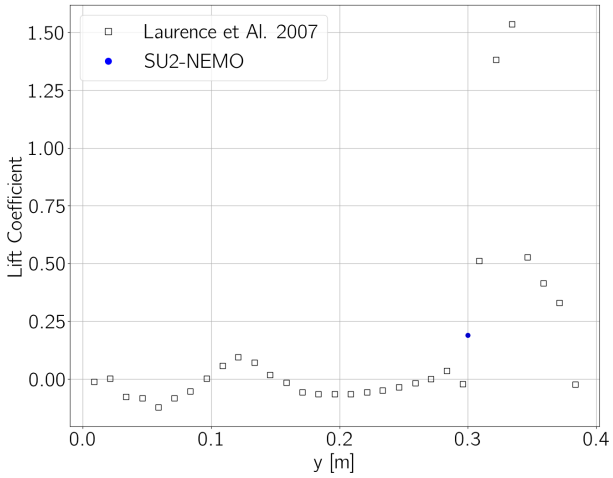

Fig. 16 Lift coefficient of the aft cylinder for a vertical displacement of 0.3 meters.

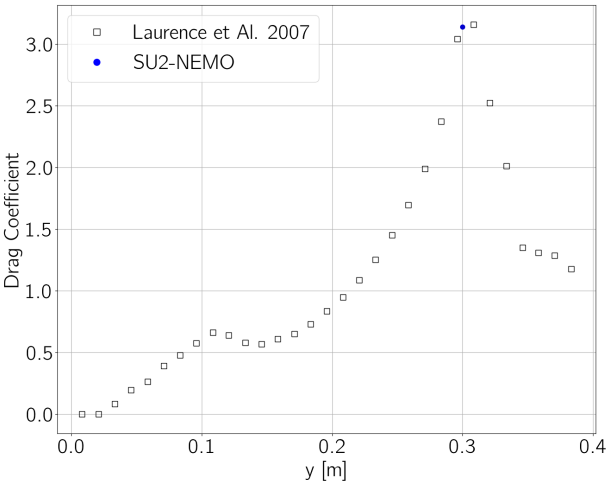

Fig. 17 Drag coefficient of the aft cylinder for a vertical displacement of 0.3 meters.

Regarding viscous simulations, normalized pressure and temperature contours are illustrated in Fig. 18 and Fig. 19, respectively. The presence of diffusivity due to viscosity resulted in the three grid contour plots to be similar, with no presence of a contact discontinuity as opposed to the inviscid case.

Analysing the heat flux profile in Fig. 15, only small discrepancies are present, with no obvious oscillations. The surface heat flux results of the structured grid have the smallest peak value, thus it is compelling to conclude that for this specific case, the anisotropic grid is not as accurate. However, it is important to remember that no adaptation was performed on the structured grid, therefore it is not possible to guarantee the orthogonality of the elements at the

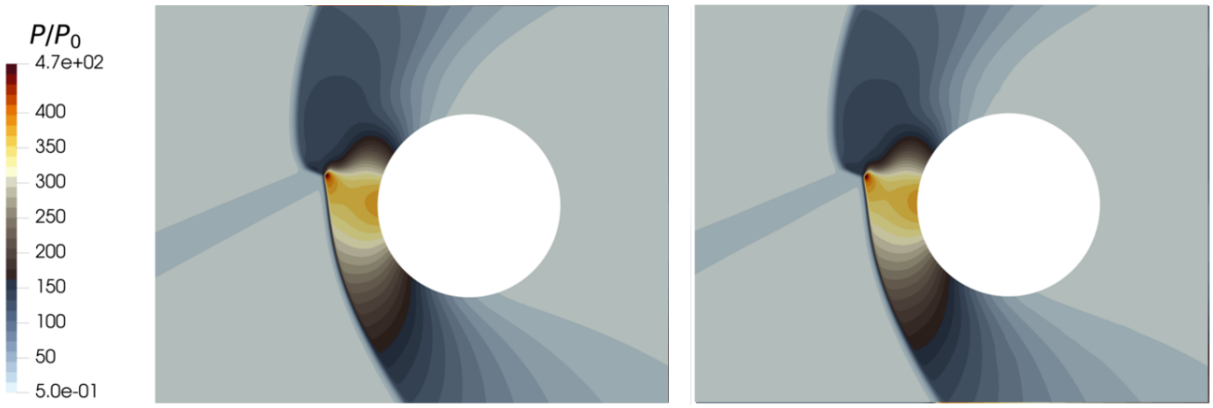

Fig. 18 Normalized pressure contours for the structured and anisotropic grids, respectively, at the shock-shock interference region using viscous formulation.

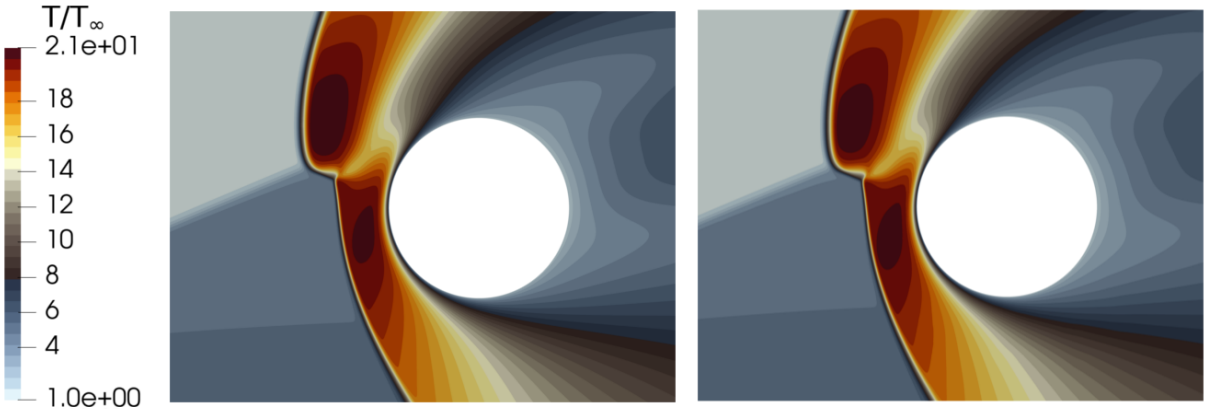

Fig. 19 Normalized temperature contours for the structured and anisotropic grids, respectively, at the shock-shock interference region using viscous formulation.

location of the shock-shock interference.

D. 3D Proximal Spheres

In this section, the effectiveness of the adaptation process for a three-dimensional viscous flow over a proximal-sphere configuration travelling at hypersonic speed is assessed. Multiple-body configurations at high-speed can be found in several situations, such as during the re-entry of fragmented objects. The configuration presented in this section enables the shock generated by the upstream sphere to interact with the bow shock generated by the presence of the downstream sphere, resulting in the formation of complex flows features that impact the forces experienced by the secondary sphere when inside the domain of influence of the primary sphere. The free-stream flow conditions, wall temperature and species mass fractions are written in Table 8, and the case geometry is illustrated in Fig. 20. The chosen conditions allowed to compare the obtained results with the experimental data from the H2K wind tunnel experiments.

Initially, an isotropic grid is used for the computation of the flowfield and prediction of the surface quantities. The final solution and numerical grid are then used to drive the adaptation process of PyAMG for the generation of the anisotropic grid. For simulations where the solution is not known beforehand, grid adaptation is necessary to achieve good predictions. Details regarding the grids used for the simulation, the computed aerodynamic coefficients and peak value of the Stanton number for the aft sphere can be found in Table 9 and the computational cost details in Table 10. The evolution of the aerodynamic coefficients and Stanton number throughout the different levels shows that the smallest difference occurs for the last grid adaptation. Additionally, it can be observed that the degree of anisotropy increases with the levels of adaptation. All the three grids employed a prismatic boundary layer around the two spheres to partially recover the solution from errors generated through the misalignment of tetrahedral elements with the shock wave. For simplicity, only the final grid used is illustrated, in Fig. 21, where a higher level of local mesh refinement and element orientation at the shock waves and shock-shock interaction region can be observed.

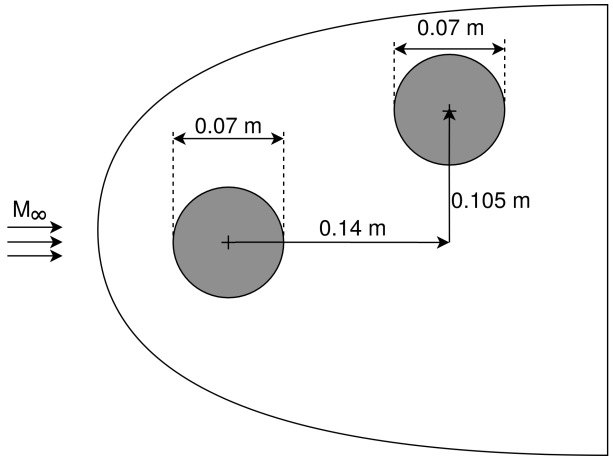

Fig. 20 Geometry configuration of the three-dimensional two-spheres case.

Table 8 Free-stream and wall values for the two-spheres case.

T_∞ $[K]$	55.56
T_w $[K]$	293.15
P_∞ $[Pa]$	125.61
U $[m/s]$	1048
N [%]	0
O [%]	0
NO [%]	0
N2 [%]	77
O2 [%]	23

Table 9 Grid details for the two-spheres case.

Grid	Nodes	Elements	Average AR	Maximum AR	C_L	C_D	St
Isotropic grid - level 0	4,834,102	12,045,150	1.553	6.313	-0.13926	0.29303	0.43858
Anisotropic grid - level 1	6,799,812	23,739,949	2.512	15.399	-0.13982	0.29383	0.19508
Anisotropic grid - level 2	8,337,524	32,954,899	4.175	48.097	-0.14196	0.29755	0.15506
Anisotropic grid - level 3	9,767,945	41,532,117	4.274	58.971	-0.14150	0.29682	0.16218

Table 10 Computational details of the two-spheres case.

Grid	Cores	CPU(h)
Isotropic grid - level 0	120	3723
Anisotropic grid - level 1	120	4245
Anisotropic grid - level 2	120	5832
Anisotropic grid - level 3	120	7310

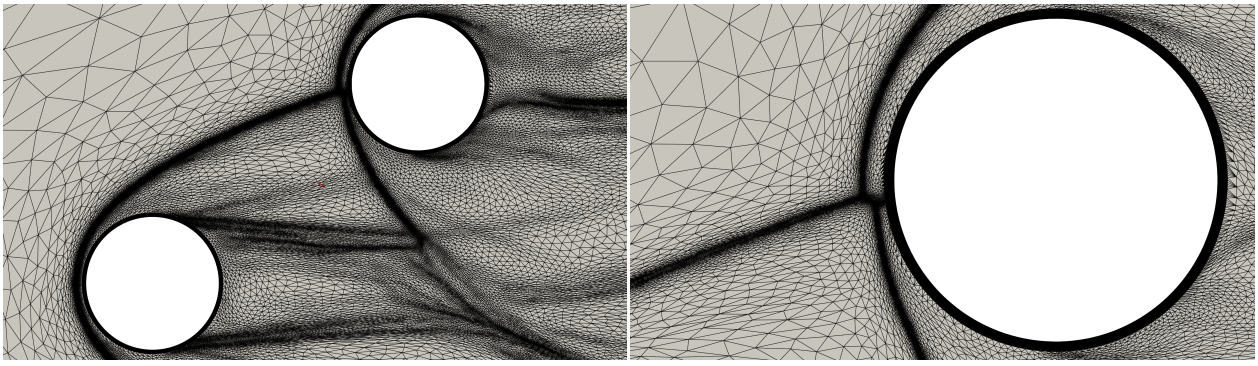

Fig. 21 Detailed visualization of the final anisotropic grid used for the two-spheres case.

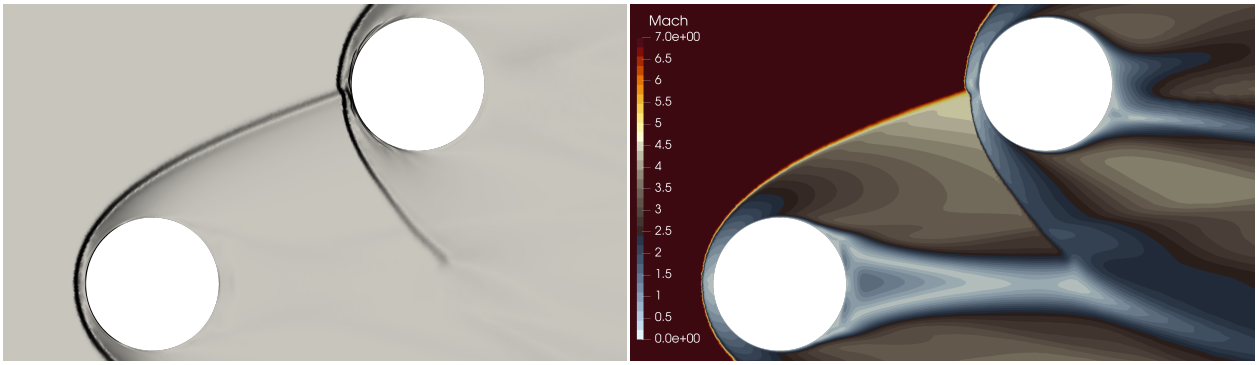

(a) Isotropic grid - level 0

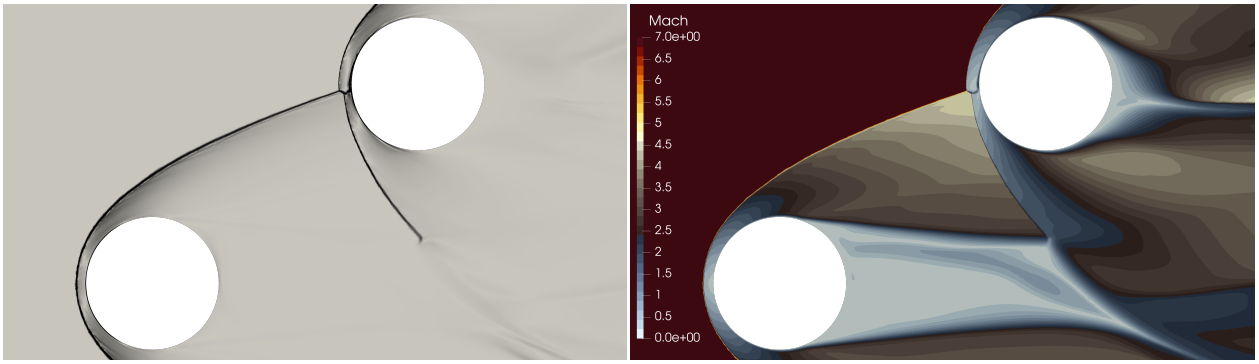

(b) Anisotropic grid - level 1

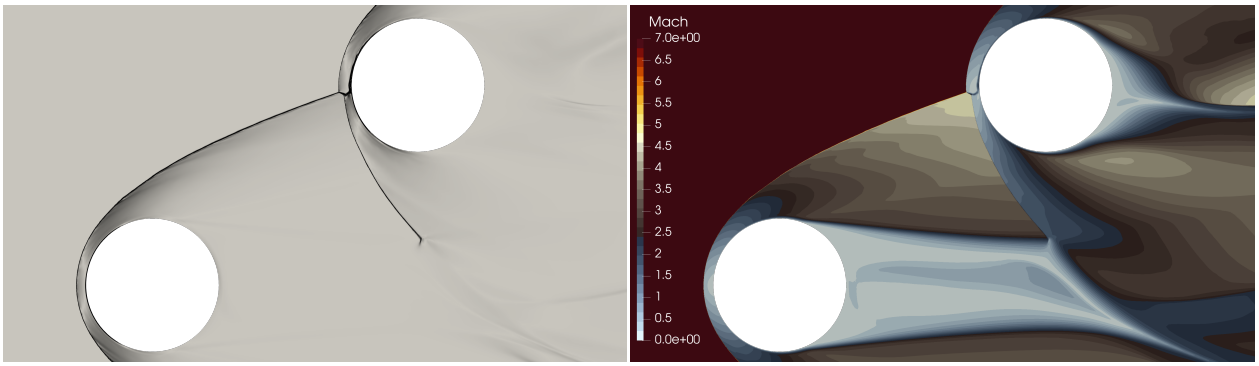

(c) Anisotropic grid - level 2

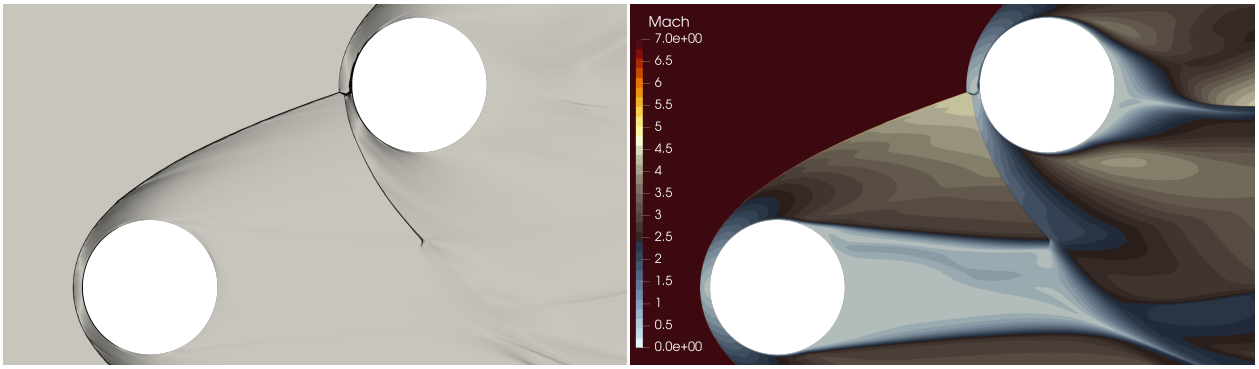

(d) Anisotropic grid - level 3

Fig. 22 Schlieren and Mach contours of the two-spheres case for different levels of adaptation.

Figure 22 shows the numerical Schlieren on the left and Mach contours on the right for the different numerical grids, starting from the isotropic grid at the top.

2It is clear that throughout the different levels of adaptation, the shock discontinuity and the shock-shock interaction pattern of type IV, according to Edney criteria [32], are sharply captured. The major flow difference can be observed when the grid is adapted for the first time, where the shock impingement on the aft sphere is captured, showing the importance of anisotropic grid adaptation and element alignment in the capture of complex features, when the solution is not known beforehand. A comparison between the numerical Schlieren of the density field gradient on the most refined anisotropic grid and the experimental Schlieren [25] obtained from experiments conducted at the hypersonic wind tunnel H2K at DLR Institute of Aerodynamics and Flow Technology is shown in Fig. 23. overlaying the Schlieren images at the region of the shock-shock interaction, it can be visualized the clear superposition of the experimental and numerical shock waves, supporting the validity of the anisotropic approach used in this work to perform proximal-body simulations.

The surface pressure plot shown in Fig. 24 illustrates the importance of grid alignment in the location of the pressure peak, where the larger difference is shown between the isotropic grid and the first adapted grid obtained. The last two grid levels show similar pressure profiles, showing that grid convergence was achieved. The obtained pressure field for the final grid, illustrated in Fig. 25, shows a smooth contour without any considerable oscillation.

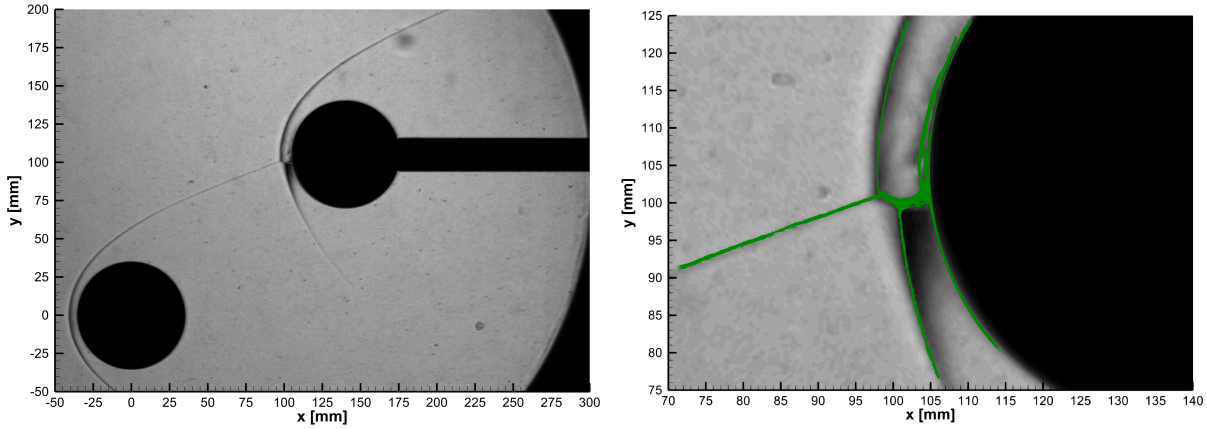

Fig. 23 Experimental Schlieren (left) and superposition of experimental and numerical Schlieren in green (right) at the shock-shock interaction region.

V. Conclusions

Accurate aerothermodynamic predictions of atmospheric re-entry of proximal objects are difficult to achieve due to the complex nature of the flow physics. The flow is characterized by highly-directional and complex flow features that require appropriate numerical treatment and multi-physics modelling for a correct prediction of the flowfield and surface aerothermodynamic quantities. The choice of element type and grid design plays an important role in the solution

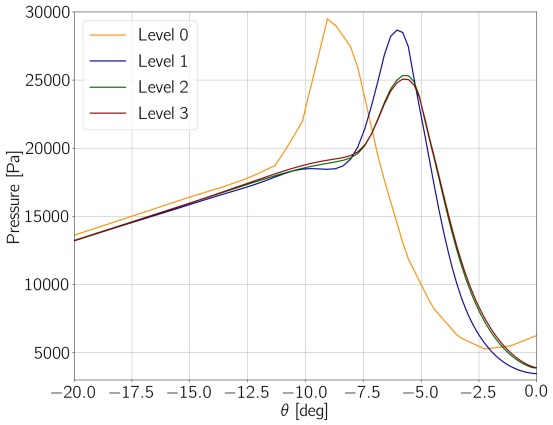

Fig. 24 Pressure plot at the symmetry plane of the aft sphere.

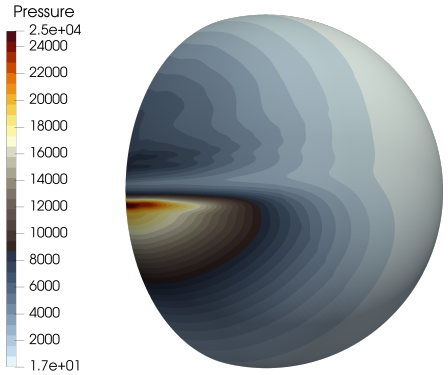

Fig. 25 Pressure contour at the surface of the aft sphere.

accuracy and numerical stability, especially when a high degree of anisotropy is considered. A common approach to achieve mesh alignment with the flow features is the use of quadrilateral/hexahedral grids, which are less inclined to give rise to numerical instabilities when compared to triangular/tetrahedral grids. Nevertheless, it is not always possible to guarantee the perfect alignment of structured grids when complex flows are established. Moreover, it is well-known that performing adaptive refinement without hanging nodes leads to unnecessary refinement in regions of uniform flow.

A numerical analysis regarding the influence of grid elements type and alignment is presented for a hypersonic AIR-5 flow with non-equilibrium effects using the SU2-NEMO solver paired with a metric-based anisotropic mesh adaptation tool. Two single-body test cases using a two-dimensional cylinder and a three-dimensional sphere were conducted. A comparison with the available literature data and with the solution obtained for structured grids (for the two-dimensional case), which are assumed to be the best practice regarding numerical grids for high-fidelity CFD simulations, reveals that results obtained with anisotropic grids provide an accurate prediction of surface aerothermodynamic quantities. The usability of anisotropic grids for the simulation of multiple proximal bodies was also assessed for proximal cylinders and proximal spheres cases, where grid adaptation show the capability of anisotropic grids to sharply capture the complex directional flow features generated by the shock-shock interaction.

Acknowledgments

The authors wish to acknowledge the support of the EPSRC funded ARCHIE-WeSt High Performance Computer (www.archie-west.ac.uk). The authors would also like to thank European Space Agency for partially funding this research and Sebastian Willems for providing experimental data for the proximal spheres case.

References

[1] Candler, G., Barnhardt, M., Drayna, T., Nompelis, I., Peterson, D., and Subbareddy, P., "Unstructured Grid Approaches for Accurate Aeroheating Simulations," *18th AIAA Computational Fluid Dynamics Conference*, 2007. doi:10.2514/6.2007-3959.

[2] Gnoffo, P., "Simulation of Stagnation Region Heating in Hypersonic Flow on Tetrahedral Grids (Invited)," *18th AIAA Computational Fluid Dynamics Conference*, 2007. doi:10.2514/6.2007-3960.

[3] Gnoffo, P., "Multi-Dimensional Inviscid Flux Reconstruction for Simulation of Hypersonic Heating on Tetrahedral Grids," *47th AIAA Aerospace Sciences Meeting including The New Horizons Forum and Aerospace Exposition*, 2009. doi:10.2514/6.2009-599.

[4] Gnoffo, P., and White, J., "Computational Aerothermodynamic Simulation Issues on Unstructured Grids," *37th AIAA Thermophysics Conference*, 2004. doi:10.2514/6.2004-2371.

[5] Nompelis, I., Drayna, T., and Candler, G., "Development of a Hybrid Unstructured Implicit Solver for the Simulation of Reacting Flows Over Complex Geometries," *34th AIAA Fluid Dynamics Conference and Exhibit*, ???? doi:10.2514/6.2004-2227.

[6] Bonfiglioli, A., Grottadaurea, M., Paciorri, R., and Sabetta, F., "An unstructured, three-dimensional, shock-fitting solver for hypersonic flows," *Computers Fluids*, Vol. 73, 2013, pp. 162–174. doi:https://doi.org/10.1016/j.compfluid.2012.12.022.

[7] Harris, M., "Flow Feature Aligned Mesh Generation and Adaptation," , April 2013.

[8] Akhlaghi, H., Roohi, E., Daliri, A., and Soltani, M.-R., "Shock polar investigation in supersonic rarefied gas flows over a circular cylinder," *Physics of Fluids*, Vol. 33, No. 5, 2021, p. 052006. doi:10.1063/5.0050571.

[9] Shoja-Sani, A., Roohi, E., and Stefanov, S., "Homogeneous relaxation and shock wave problems: Assessment of the simplified and generalized Bernoulli trial collision schemes," *Physics of Fluids*, Vol. 33, No. 3, 2021, p. 032004. doi:10.1063/5.0039071.

[10] Economon, T. D., Palacios, F., Copeland, S. R., Lukaczyk, T. W., and Alonso, J. J., "SU2: An Open-Source Suite for Multiphysics Simulation and Design," *AIAA Journal*, Vol. 54, No. 3, 2016, pp. 828–846. doi:10.2514/1.J053813.

[11] Palacios, F., Copeland, S., Lonkar, A., and Alonso, J., "Adjoint-Based Goal-Oriented Mesh Adaptation for Nonequilibrium Hypersonic Flows," *51st AIAA Aerospace Sciences Meeting including the New Horizons Forum and Aerospace Exposition, Grapevine, TX. AIAA Paper 2013-0552*, 2013. doi:10.2514/6.2013-552.

[12] Maier, W. T., Needels, J. T., Garbacz, C., Morgado, F., Alonso, J. J., and Fossati, M., "SU2-NEMO: An Open-Source Framework for High-Mach Nonequilibrium Multi-Species Flows," *Aerospace*, Vol. 8, No. 7, 2021. 10.3390/aerospace8070193.

[13] Scoggins, J., and Magin, T., "Development of Mutation++: Multicomponent Thermodynamic and Transport Properties for Ionized Plasmas written in C++," 2014. doi:10.2514/6.2014-2966.

[14] Garbacz, C., Maier, W., Scoggins, J., Economon, T. D., Magin, T., Alonso, J. J., and Fossati, M., "Shock interactions in inviscid air and CO_2-N_2 flows in thermochemical non-equilibrium," *Shock Waves*, 2021. doi:10.1007/s00193-021-00999-8.

[15] Park, C., "Review of chemical-kinetic problems of future NASA missions. I - Earth entries," *Journal of Thermophysics and Heat Transfer*, Vol. 7, No. 3, 1993, pp. 385–398. doi:10.2514/3.431.

[16] Kim, K. H., Kim, C., and Rho, O.-H., "Methods for the Accurate Computations of Hypersonic Flows: I. AUSMPW+Scheme," *Journal of Computational Physics*, Vol. 174, No. 1, 2001, pp. 38–80. doi:https://doi.org/10.1006/jcph.2001.6873.

[17] Liou, M.-S., "A sequel to AUSM, Part II: AUSM+-up for all speeds," *Journal of Computational Physics*, Vol. 214, No. 1, 2006, pp. 137–170. doi:https://doi.org/10.1016/j.jcp.2005.09.020.

[18] sheng Chen, S., Yan, C., xi Lin, B., yuan Liu, L., and Yu, J., "Affordable shock-stable item for Godunov-type schemes against carbuncle phenomenon," *Journal of Computational Physics*, Vol. 373, 2018, pp. 662–672. doi:https://doi.org/10.1016/j.jcp.2018.07.022.

[19] Loseille, A., and Loehner, R., "Boundary Layer Mesh Generation and Adaptivity," 2011. doi:10.2514/6.2011-894.

[20] Loseille, A., and Menier, V., "Serial and Parallel Mesh Modification Through a Unique Cavity-Based Primitive," *Proceedings of the 22nd International Meshing Roundtable*, edited by J. Sarrate and M. Staten, Springer International Publishing, Cham, 2014, pp. 541–558. doi:10.1007/978-3-319-02335-9_30.

[21] Loseille, A., Menier, V., and Alauzet, F., "Parallel Generation of Large-size Adapted Meshes," *Procedia Engineering*, Vol. 124, 2015, pp. 57 – 69. doi:10.1016/j.proeng.2015.10.122, 24th International Meshing Roundtable.

[22] Vallet, M.-G., Manole, C.-M., Dompierre, J., Dufour, S., and Guibault, F., "Numerical comparison of some Hessian recovery techniques," *International Journal for Numerical Methods in Engineering*, Vol. 72, No. 8, 2007, pp. 987–1007.

[23] Frazza, L., "3D anisotropic mesh adaptation for Reynolds Averaged Navier-Stokes simulations," Theses, Sorbonne Université, Dec. 2018. URL `https://tel.archives-ouvertes.fr/tel-02887880`.

[24] Loseille, A., "Unstructured Mesh Generation and Adaptation," *Handbook of Numerical Methods for Hyperbolic Problems - Applied and Modern Issues*, edited by R. Abgrall and C.-W. Shu, Elsevier, 2017, pp. 263–302. doi:10.1016/bs.hna.2016.10.004.

[25] Sebastian Willems, A. G., Patrick Seltner, "Shock-Shock Interaction Test Case," *ESA ATD3 Workshop*, 2018.

[26] Carpenter, M. H., and Casper, J. H., "Accuracy of Shock Capturing in Two Spatial Dimensions," *AIAA Journal*, Vol. 37, No. 9, 1999, pp. 1072–1079. doi:10.2514/2.835.

[27] Knight, D., Longo, J., Drikakis, D., Gaitonde, D., Lani, A., Nompelis, I., Reimann, B., and Walpot, L., "Assessment of CFD capability for prediction of hypersonic shock interactions," *Progress in Aerospace Sciences*, Vol. 48-49, 2012, pp. 8–26. doi:https://doi.org/10.1016/j.paerosci.2011.10.001, assessment of Aerothermodynamic Flight Prediction Tools.

[28] Geuzaine, C., and Remacle, J.-F., "Gmsh: A 3-D finite element mesh generator with built-in pre- and post-processing facilities," *International Journal for Numerical Methods in Engineering*, Vol. 79, No. 11, 2009, pp. 1309–1331. doi:https://doi.org/10.1002/nme.2579.

[29] Karl, S., Schramm, J. M., and Hannemann, K., "High Enthalpy Cylinder Flow in HEG: A Basis for CFD Validation," *33rd AIAA Fluid Dynamics Conference and Exhibit*, 2003, p. 4252. doi:10.2514/6.2003-4252.

[30] Yamamoto, S., Takasu, N., and Nagatomo, H., "Numerical Investigation of Shock/Vortex Interaction in Hypersonic Thermochemical Nonequilibrium Flow," *Journal of Spacecraft and Rockets*, Vol. 36, No. 2, 1999, pp. 240–246. doi:10.2514/2.3438.

[31] Laurence, S., Deiterding, R., and Hornung, H., "Proximal bodies in hypersonic flow," *Journal of Fluid Mechanics*, Vol. 590, 2007, pp. 209 – 237.

[32] Edney, B., "Anomalous Heat Transfer and Pressure Distributions on Blunt Bodies at Hypersonic Speeds in the Presence of an Impinging Shock," 1968. Report 115. Flygtekniska Foroksanstalten, Stockholm: The Aeronautical Research Institute of Sweden.